Nano Research 2018, 11(7): 3844–3853
https://doi.org/10.1007/s12274-017-1958-8
Research Article

ISSN 1998-0124
CN 11-5974/O4

MoS_2 embedded in 3D interconnected carbon nanofiber film as a free-standing anode for sodium-ion batteries

Hai Yang[1], Min Wang[1], Xiaowu Liu[1], Yu Jiang[1], and Yan Yu[1,2] (✉)

[1] *CAS Key Laboratory of Materials for Energy Conversion, Department of Materials Science and Engineering, University of Science and Technology of China, Hefei 230026, China*
[2] *State Key Laboratory of Fire Science, University of Science and Technology of China, Hefei 230026, China*

Received: 26 September 2017
Revised: 14 November 2017
Accepted: 10 December 2017

KEYWORDS

MoS_2, sodium ion battery, flexible electrode, three-dimensional (3D) interconnected carbon nanofiber

ABSTRACT

As a typical two-dimensional transition metal dichalcogenide, molybdenum disulfide (MoS_2) is considered a potential anode material for sodium-ion batteries (NIBs), due to its relatively high theoretical capacity (~ 670 $mAh \cdot g^{-1}$). However, the low electrical conductivity of MoS_2 and its dramatic volume change during charge/discharge lead to severe capacity degradation and poor cycling stability. In this work, we developed a facile, scalable, and effective synthesis method to embed nanosized MoS_2 into a thin film of three-dimensional (3D)-interconnected carbon nanofibers (CNFs), producing a MoS_2/CNFs film. The free-standing MoS_2/CNFs thin film can be used as anode for NIBs without additional binders or carbon black. The MoS_2/CNFs electrode exhibits a high reversible capacity of 260 $mAh \cdot g^{-1}$, with an extremely low capacity loss of 0.05 $mAh \cdot g^{-1}$ per cycle after 2,600 cycles at a current density of 1 $A \cdot g^{-1}$. This enhanced sodium storage performance is attributed to the synergistic effect and structural advantages achieved by embedding MoS_2 in the 3D-interconnected carbon matrix.

1 Introduction

Over the past three decades, lithium-ion batteries (LIBs) have been extensively applied in various energy storage systems, such as portable electronic devices, electrical vehicles, and smart grids, owing to their high specific capacity, absence of memory effects, and high energy density [1–3]. Nevertheless, the high cost and the geographical distribution of lithium sources in the earth crust have limited the large-scale application of LIBs [4, 5]. Recently, sodium-ion batteries (NIBs) have attracted increasing attention because of their low cost and the ubiquitous distribution of sodium salts [6–8]. Unfortunately, the anode material used in commercial LIBs, graphite, cannot be directly employed as anode for NIBs, because of the larger ionic radius of Na (0.102 nm) compared to Li (0.076 nm) [7, 9, 10], which makes it difficult to accommodate the insertion/extraction of sodium ions in the graphite interlayer. This has prompted new studies aimed at identifying advanced anode materials for NIBs, including carbon-based materials [11–13], phosphorus [14–16], metallic

---

Address correspondence to yanyumse@ustc.edu.cn

alloys [17–20], two-dimensional (2D) metal carbides (MXenes) [21, 22], and other materials [23, 24]. Among these systems, carbon-based and MXene materials deliver low capacities (less than 300 mAh·g^{-1}) [11]. Alloy anodes have high theoretical capacities, but most of them exhibit poor cycle life as a consequence of extremely large volume changes during sodium ion insertion/extraction.

Layered 2D molybdenum disulfide (MoS_2) was recently applied in a wide range of fields, including hydrogen storage [25], electrocatalysis, [26], optoelectronic transistors [27], and LIBs [28, 29]. As a representative transition metal dichalcogenide, bulk MoS_2 consists of S–Mo–S layers, in which Mo atoms are sandwiched between S atoms through strong covalent bonds while the 2D sandwich layers are stacked together through weak van der Waals interactions. The distance between neighboring layers is about 0.62 nm [30], which is much higher than that of graphite (0.34 nm). Recently, MoS_2 materials with different morphologies have been applied as anodes for LIBs, showing a very high theoretical capacity (~ 670 mAh·g^{-1}) based on the conversion reaction mechanism [28, 29, 31]. Due to the similarity of the chemical reactions involving Li and Na, MoS_2 could also be used as anode material for NIBs. The first study of the electrochemical properties of MoS_2 for NIBs was conducted by the Park's group in 2013 [32]. Commercial MoS_2 delivers a low discharge capacity of 85 mAh·g^{-1} at 0.4–2.6 V after 100 cycles, based on the intercalation reaction. In order to obtain a higher capacity, the cutoff discharge potential can be shifted to lower voltages (0.01 V), resulting in an increase in the capacity of MoS_2 via a four-electron conversion reaction of MoS_2 to Mo and Na_2S [33]. In addition, pure MoS_2 usually exhibits poor rate capability and a rapid capacity decrease due to the low electronic conductivity of MoS_2 and the huge volume change during sodiation/desodiation processes [34, 35].

Current strategies to overcome the above volume change and electronic conductivity issues are based on designing different MoS_2 morphologies [36–39]. The fabrication of electrode architectures based on MoS_2/carbon hybrid nanostructures is considered an effective solution to improve the electronic conductivity and structural stability of MoS_2 [28, 35, 40]. The Lee's group prepared MoS_2–carbon monolayer sandwiched nanosheets through a solvothermal method; the as-prepared samples exhibited an extraordinary discharge capacity of 620 mAh·g^{-1} at 0.2 A·g^{-1}, and retained capacities of 477 and 415 mAh·g^{-1} at 0.2 and 1 A·g^{-1}, respectively, over 200 cycles [41]. Zhang et al. prepared hollow MoS_2@C nanotube composites through a facile hydrothermal process; the synthesized compounds showed an enhanced initial discharge capacity of 640 mAh·g^{-1} at 0.5 C and a capacity retention of 80% after 200 cycles at a rate of 0.5 C [35]. Recently, Park et al. synthesized few-layer MoS_2 incorporated into hierarchical porous carbon nanosheet composites, which delivered a reversible capacity of 280 mAh·g^{-1} after 300 cycles at 1 A·g^{-1} for NIBs [42].

In order to further enhance the performance by combining the approaches discussed above, we designed a new type of MoS_2-based hybrid nanostructures. This system consists of MoS_2 nanoparticles uniformly embedded in a three-dimensional (3D) interconnected carbon nanofiber (CNF) film (the resulting composite film is denoted as MoS_2/CNFs in the following), as a free-standing and binder-free anode for sodium-ion batteries. We developed a facile and easy scalable process to prepare MoS_2/CNFs thin films using a common biomass material (bacterial cellulose, BC) as the carbon source [43–45]. The unique approach developed here is cost-effective and industrially viable, which are important requisites for its practical application. The present structures exhibit several desirable properties, including a highly porous and continuous conductive 3D network, which can not only enhance the diffusion kinetics of both ions and electrons, but also buffer the volume change of MoS_2. The obtained free-standing MoS_2/CNFs thin film was directly applied as a flexible electrode for NIBs, and resulted in a fairly high initial specific capacity of 617 mAh·g^{-1} at 0.1 A·g^{-1}, and a well-maintained capacity of 260 mAh·g^{-1} at 1 A·g^{-1} after 2,600 cycles. This scalable fabrication method and advantageous nanostructure make it versatile to a wide range of alloy-type anode materials towards improved battery performance.

2 Experimental

2.1 Materials synthesis

BC membranes were purchased directly from Hainan

Yeguo Foods Co., Ltd. After cutting them into small pieces using a knife, the membranes were immersed in 20 mM ammonium tetrathiomolybdate (ATM) aqueous solution for 2 days. Subsequently, the samples were frozen in liquid nitrogen and freeze-dried for 48 h. The dry BC/ATM aerogel was pyrolyzed at 800 °C for 2 h in N_2 atmosphere with a heating rate of 5 °C·min^{-1}. The MoS_2/CNFs samples were obtained after cooling to room temperature in a tubular furnace. CNF slices were prepared by a similar method to that used for the MoS_2/CNFs, with the exception that BC was only immersed in ultrapure water, without any additives.

2.2 Materials characterization

X-ray diffraction (XRD) measurements were carried out on a Philips X'Pert Pro Super diffractometer with Cu Kα radiation. Raman spectra were obtained using a Thermo Scientific DXR microscope with a 532 nm laser. X-ray photoelectron spectroscopy (XPS) measurements were performed on a Thermo VG Scientific instrument. Nitrogen adsorption/desorption isotherms were determined by an ASAP 2020 accelerated surface area and porosimetry system. The carbon content of the MoS_2/CNFs samples was determined by thermogravimetric analysis (TGA) using a TGA Q5000 instrument. The microstructure of the samples was analyzed by field-emission scanning electron microscopy (FESEM, JSM-6700) and transmission electron microscopy (TEM, JEOL 4000EX).

2.3 Electrochemical characterization

The as-obtained flexible MoS_2/CNFs film was cut into small pieces (~ 1 cm × 1 cm, 2–2.2 mg·cm^{-2} mass loading), and directly used as electrode plate without subsequent processing. Standard CR2032 coin cells were fitted together in a high-purity argon-filled glovebox using sodium film as both reference and counter electrode. The MoS_2/CNFs and sodium films were immersed in the electrolyte, composed of 1 M $NaClO_4$ in ethylene carbonate (EC), dimethyl carbonate (DMC), and fluoroethylene carbonate (FEC) with EC:DMC:FEC = 1:1:0.05 volume ratios. Whatman glass fiber was used as the separator. Galvanostatic charge/discharge curves were measured by a Neware BTS-610 instrument at voltages ranging from 0.01 to 3 V. Cyclic voltammetry (CV) curves were acquired on a CHI 660D electrochemical workstation.

3 Results and discussion

The synthesis of the free-standing and flexible MoS_2/CNFs films is illustrated in Fig. 1(a). First, the BC membranes were immersed in 20 mM ATM aqueous solution for 48 h under magnetic stirring at room temperature, to allow continuous absorption of ATM until saturation. Dried BC/MoS_2 aerogels were obtained after removing water by freeze-drying. Finally, the dried MoS_2/ATM aerogels were carbonized in a tubular furnace under N_2 atmosphere. During the carbonization process, MoS_2 nanoparticles were generated from ATM and embedded in the carbon nanofibers. The flexible MoS_2/CNFs thin film can be used as a free-standing and flexible anode for NIBs (Figs. 1(b) and 1(c)).

The morphology and microstructure of the CNFs and MoS_2/CNFs samples were investigated by scanning electron microscopy (SEM) and TEM measurements. Figures S1(a)–S1(d) in the Electronic Supplementary Material (ESM) show the morphology of the pure CNFs, whose structure consists of 3D-interconnected fibers. Figure 2 shows the microstructure of the MoS_2/CNFs, which display a similar morphology to the CNFs. The as-obtained MoS_2/CNFs pellicles exhibit a 3D interconnected structure, in which each nanofiber

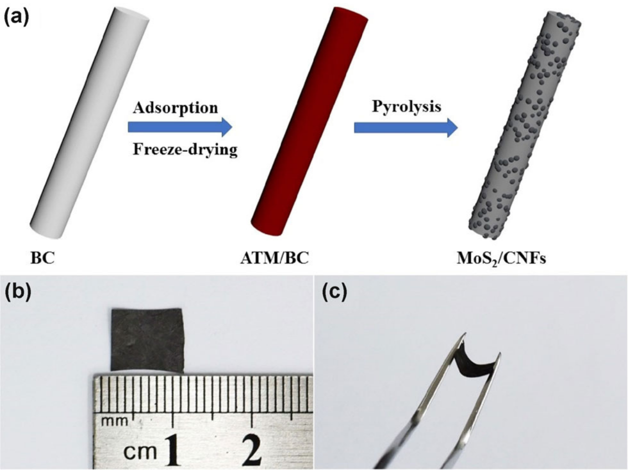

Figure 1 (a) Schematic illustration of the synthesis process of MoS_2/CNFs. (b) and (c) Photographs of the free-standing and flexible MoS_2/CNFs electrode.

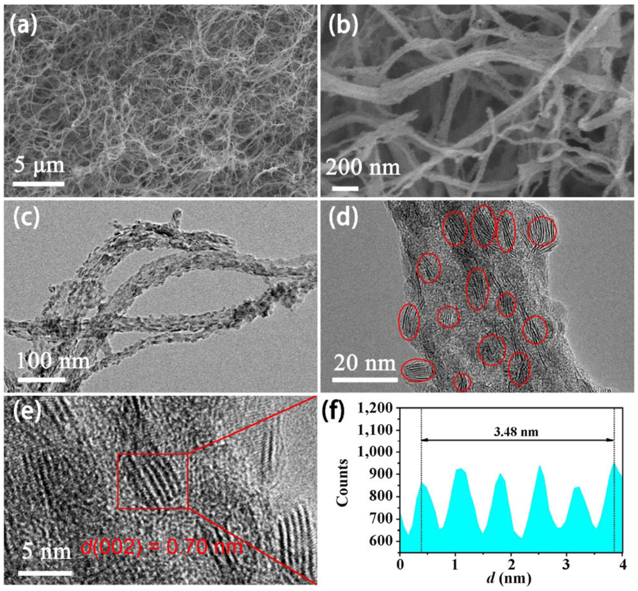

Figure 2 Structural characterization of MoS_2/CNFs. (a) and (b) SEM images; (c) TEM image; (d) and (e) HRTEM images; (f) line profile corresponding to the framed area in (e).

is around 20–80 nm in diameter and tens of micrometers in length (Figs. 2(a)–2(c)). The MoS_2/CNFs exhibited a rougher surface compared to the CNFs, due to the MoS_2 nanoparticles embedded in the carbon nanofibers. Figure S2 in the ESM shows a cross-section SEM image of the MoS_2/CNFs film, whose thickness is about 200 μm. The TEM image of the MoS_2/CNFs (Fig. 2(c)) confirms the roughness of their surface, in agreement with the SEM result. The high-resolution TEM (HRTEM) image in Fig. 2(d) highlights the core–shell structure of the MoS_2/CNFs, in which the MoS_2 particles formed *in situ* are uniformly dispersed in the CNFs matrix. The average size of the MoS_2 nanoparticles is ~ 10 nm. Figure 2(e) displays an enlarged view of the MoS_2 nanoparticles, showing that the interlayer distance between crystalline MoS_2 sheets is 0.70 nm (according to the statistics in Fig. 2(f)), corresponding to the (002) planes of hexagonal MoS_2. This interlayer separation is larger than that of standard bulk MoS_2 (0.62 nm) [30, 46]. The expanded interlayer of the present samples could provide more room for sodium ion transport. Furthermore, the 3D-interconnected porous carbon matrix derived from carbonization of BC can also accelerate electron and ion transport.

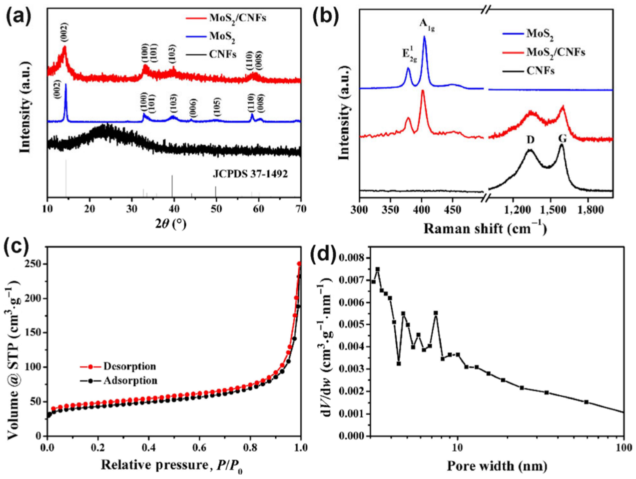

Figure 3 (a) XRD patterns and (b) Raman spectra of MoS_2, CNFs, and MoS_2/CNFs; (c) N_2 absorption–desorption isotherms; (d) pore distributions of the MoS_2/CNFs.

The XRD patterns of MoS_2, CNFs, and MoS_2/CNFs are displayed in Fig. 3(a). Obviously, the main diffraction peaks of MoS_2 and MoS_2/CNFs match well those of the 2H-MoS_2 structure (JCPDS 37-1492) [28, 47]. The carbon content of as-synthesized MoS_2/CNFs was determined by TGA (Fig. S3 in the ESM). During the TGA tests in air, the carbon in the MoS_2/CNFs sample would burn when the temperature exceeds 300 °C, while MoS_2 is oxidized to MoO_3 [40, 42]. Based on the 34.1% mass loss of MoS_2/CNFs between 300 and 450 °C, the corresponding MoS_2 and carbon contents are 73.2% and 26.8%, respectively. The prepared samples were further analyzed by Raman spectroscopy, and the results are shown in Fig. 3(b). Raman peaks at 379 and 402 cm^{-1} are associated to the E^1_{2g} (in-plane) and A_{1g} (out-of-plane) vibrational modes of 2H-MoS_2 [48, 49], respectively. Moreover, the two broad peaks located at 1,360 and 1,598 cm^{-1} correspond to the D and G modes of carbon, respectively [50, 51], further confirming the presence of carbon and 2H-MoS_2 in the as-obtained composites. The porous nature of the MoS_2/CNFs was probed by nitrogen adsorption–desorption analysis (Fig. 3(c)), whereas Fig. 3(d) displays the corresponding pore size distribution. A surface area of 158 $m^2 \cdot g^{-1}$ was estimated using the Brunauer–Emmett–Teller (BET) equation, along with a 2–10 nm mesoporous distribution, which is beneficial for sodium-ion diffusion and electrolyte infiltration.

The XPS analysis was used to determine the composition and chemical environment of elements present in the MoS_2/CNFs composite (Fig. 4). The typical sharp peaks of Mo 4p, Mo 4s, S 2p, Mo 3d, C 1s, Mo 3p, and O 1s species can be clearly seen

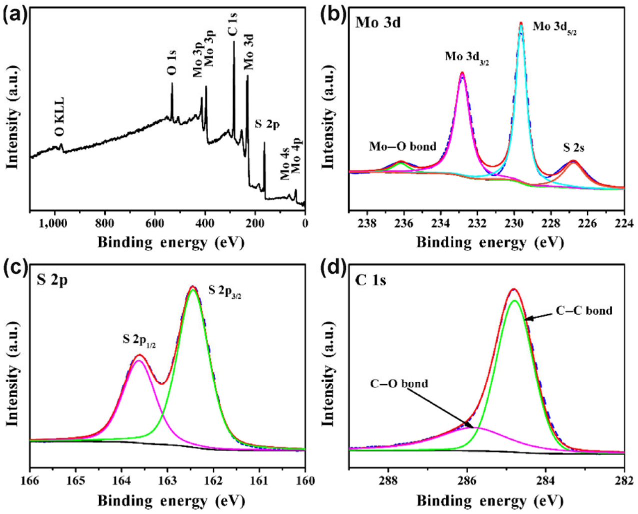

Figure 4 (a) XPS spectrum of MoS_2/CNFs; (b)–(d) high-resolution XPS spectra of Mo 3d, S 2p, and C 1s.

in Fig. 4(a), indicating that the MoS_2/CNFs composite contains Mo, S, C, and O atoms [29, 52]. Figures 4(b)–4(d) display the high-resolution spectra of Mo 3d, S 2p, and C 1s, respectively. The Mo $3d_{3/2}$ and $3d_{5/2}$ peaks located at 232.82 and 229.62 eV, respectively, reveal the presence of Mo^{4+} in the MoS_2/CNFs composite [41, 53]. Moreover, the peak at 236.17 eV can be assigned to the Mo^{6+} species in MoO_3, formed by surface oxidation of the product by oxygen in air [42]. A small broad peak at a binding energy of 226.75 eV is attributed to the S 2s spectrum of MoS_2. In addition, two peaks at 162.62 and 163.62 eV can be observed in the high-resolution S spectra, corresponding to S $2p_{3/2}$ and $2p_{1/2}$, respectively [54, 55]. The C 1s spectrum can be easily resolved into two peaks centered at 284.82 and 286.52 eV, corresponding to C–C and C–O bonds, respectively [56]. The presence of oxygen derives from the incomplete carbonization of BC [43, 45]. The high-angle annular dark-field scanning transmission electron microscopy (HAADF-STEM) image and elemental mappings of Mo, S, C, and O (Fig. 5) clearly indicate that the MoS_2 nanoparticles were well-proportioned distributed in the MoS_2/CNFs composites.

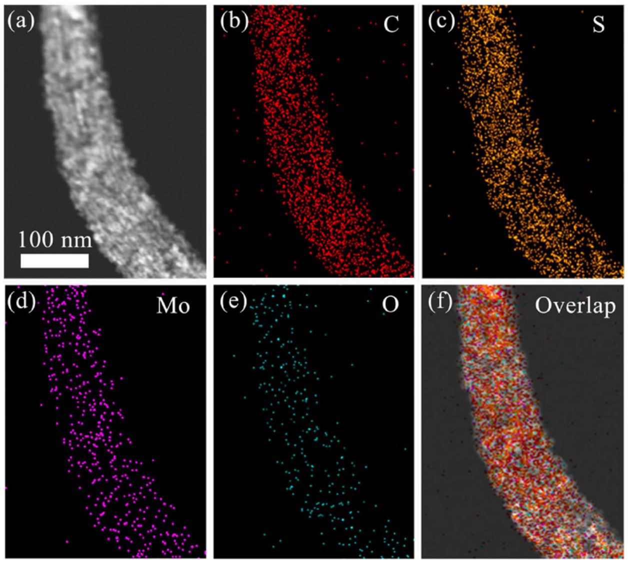

Figure 5 HAADF-STEM image of MoS_2/CNFs (a) and corresponding elemental mappings: (b) C, (c) S, (d) Mo, (e) O, and (f) overlap of elements.

Next, we assessed the performance of the as-prepared free-standing MoS_2/CNFs films as electrodes for NIBs. Figure 6(a) shows the CV profiles of MoS_2/CNFs recorded in the first three cycles, in the voltage window of 0.01–3 V vs. Na^+/Na and at a scan rate of 0.1 mV·s^{-1}. Three pronounced cathodic peaks at 1.02, 0.80, and 0.01 V are observed in the first discharge process. The first irreversible peak at about 1.02 V is attributed to the decomposition of the electrolyte, accompanied by formation of the solid/electrolyte interphase (SEI) [40, 47]. The second peak at 0.8 V originates from the stepwise intercalation reaction between MoS_2 and sodium ions, to form Na_xMoS_2 [40, 41]. The third deep peak between 0.3 and 0.01 V is assigned to the conversion reaction to form metallic Mo and Na_2S, together with sodium intercalation into the interlayer of carbon [42, 46]. Subsequently, a broad peak observed between 1.4 and 1.9 V during the first charge process could be ascribed to a reversible phase transition to MoS_2 [41, 42]. After the first charge/discharge process, the redox peaks become broader and unapparent, due to the amorphization of crystalline MoS_2 during the charge/discharge process. Remarkably, the CV curves remain almost unchanged after the first cycle, demonstrating the excellent stability of the MoS_2/CNFs electrode.

Figure 6(b) displays the galvanostatic charge–discharge profiles of the MoS_2/CNFs at a current rate of 0.1 A·g^{-1}. The initial discharge and charge specific capacities are 1,238 and 617 mAh·g^{-1}, respectively, corresponding to an initial Coulombic efficiency (ICE) of 50%. The large irreversible capacity can be attributed not only to the electrolyte decomposition at the electrode surface to form the SEI film, but also to the

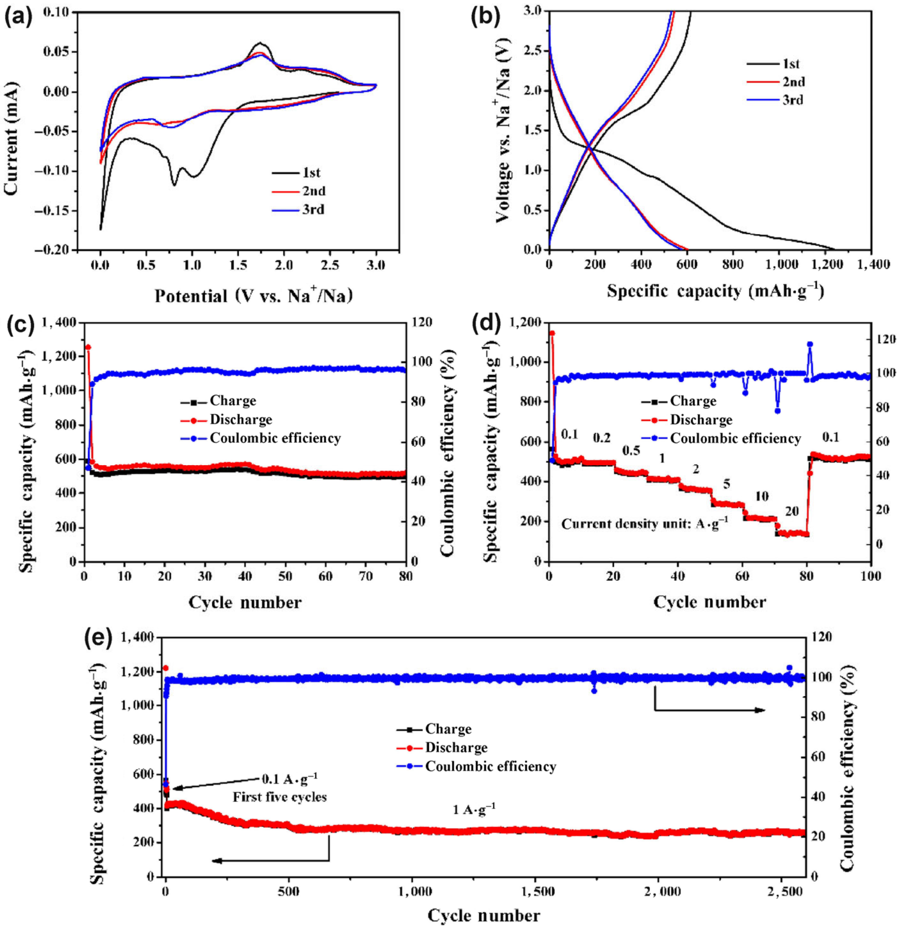

Figure 6 Electrochemical measurements for MoS_2/CNFs. (a) CV curves for the first three cycles at a scan rate of 0.1 mV·s^{-1}. (b) Galvanostatic charge/discharge curves for the first three cycles at 0.1 A·g^{-1}. (c) Cycling stability at 0.1 A·g^{-1}. (d) Rate capability at different specific currents. (e) Long-term cycling stability at 1 A·g^{-1} with five-cycle activation at a low current density of 0.1 A·g^{-1}.

irreversible reaction of sodium ions with MoS_2 and carbon [35, 40]. The cycling stability of the MoS_2/CNFs at 0.1 A·g^{-1} is illustrated in Fig. 6(c). The electrode delivers a high specific capacity of about 500 mAh·g^{-1} after 80 charge–discharge cycles. As a reference, the cycling performance of CNFs and MoS_2 are shown in Fig. S5 in the ESM. The first discharge and charge capacities of CNFs at 0.1 A·g^{-1} are 1,265 and 215 mAh·g^{-1}, respectively. The CNFs maintain a reversible capacity of 167 mAh·g^{-1} for 80 cycles, while MoS_2 shows poor reversible capacity (94 mAh·g^{-1} after 80 cycles). It can be concluded that embedding MoS_2 in CNFs considerably improves not only the specific capacity, but also the cycling stability. Figure 6(d) shows the rate capability of the MoS_2/CNFs. The reversible capacity decreases very slowly with increasing current density: The measured discharge capacities are 500, 488, 440, 410, 360, 285, and 210 mAh·g^{-1} at 0.1, 0.2, 0.5, 1, 2, 5, 10, and 20 A·g^{-1}, respectively. In addition, when the current density is reduced back to 0.1 A·g^{-1}, a high charge specific capacity of 510 mAh·g^{-1} is rapidly recovered. In contrast, pure CNFs show a low specific capacity when tested under the same conditions (see Figs. S3–S5 in the ESM).

To further evaluate the long-term cycle life of the MoS_2/CNFs, the cell was cycled at 1 A·g^{-1} for 2,600 cycles: As shown in Fig. 6(e), the electrode delivers a stable reversible capacity of 260 mAh·g^{-1} with an extremely low capacity loss of 0.05 mAh·g^{-1} per cycle. To inspect possible structural changes in MoS_2/CNFs after the long-term cycling, we performed SEM and HRTEM measurements to determine the morphology of the composites after 2,600 cycles at 1 A·g^{-1}. Figure 7(a) confirms that the nanofiber

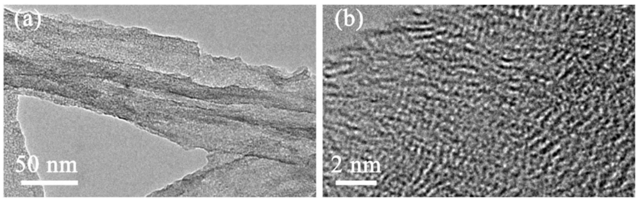

Figure 7 (a) TEM and (b) HRTEM images of MoS_2/CNFs after 2,600 cycles at a current density of 1 A·g^{-1}.

structure remains intact. The HRTEM image (Fig. 7(b)) reveals the presence of amorphous MoS_2 and porous carbon rather than crystalline 2H-MoS_2 before the electrochemical sodiation process, due to the conversion reaction. Moreover, the SEM images of the MoS_2/CNFs composite at the first discharge state and the charge state of the first and 100th cycles are shown in Fig. S6 in the ESM. Compared with the original morphology, the surface of the nanofibers becomes covered by a stable SEI film after the first discharge process. Even at the 100th cycle, the MoS_2/CNFs electrode maintains a 3D interconnected network structure without any broken.

The improved electrochemical performance of the present MoS_2/CNFs electrodes can be attributed to the synergistic effect and structural advantages of embedding MoS_2 in the 3D-interconnected carbon matrix, which produces the following benefits: (1) The 3D interconnected carbon nanofibers possess a large surface area and high mechanical flexibility, providing a 3D-interconnected electronic and ionic pathway for fast charge transfer and ion diffusion; (2) the CNFs matrix can buffer the volume change of MoS_2 during sodiation/desodiation processes, leading to long cycle life and outstanding rate capability.

4 Conclusions

In order to enhance the performance of MoS_2 electrodes, we have rationally designed and synthesized a flexible and free-standing MoS_2/CNFs film by using a typical biomass material (bacterial cellulose) as carbon source. The present fabrication process is facile, environmentally friendly, and easy to scale up. The MoS_2/CNFs electrodes show a 3D interconnected network structure, in which MoS_2 nanoparticles are encapsulated in the porous carbon nanofibers. The robust structure and highly conductive network make the MoS_2/CNFs composite an ideal free-standing anode for NIBs. In fact, the electrode delivers an excellent cycling stability (260 mAh·g^{-1} after 2,600 cycles at 1 A·g^{-1}) and rate performance (210 mAh·g^{-1} at 20 A·g^{-1}). The carbon network not only provides superior electrical conductivity, but can also accommodate volume changes and improve ion transport. The present synthetic strategy should be extendable to fabricate other 2D materials encapsulated into flexible and free-standing 3D carbon networks, with potential application in energy storage and catalysis fields.

Acknowledgments

This work was supported by the National Key Research and Development Program of China (No. 2016YFB0100305), the National Natural Science Foundation of China (Nos. 21373195 and 51622210), the Fundamental Research Funds for the Central Universities (No. WK3430000004), and the Collaborative Innovation Center of Suzhou Nano Science and Technology.

Electronic Supplementary Material: Supplementary material (SEM images of CNFs, TG curves, CV curves, *ex suit* SEM, *ex suit* XRD and electrochemical performance of CNFs) is available in the online version of this article at https://doi.org/10.1007/s12274-017-1958-8.

References

[1] Dunn, B.; Kaamath, H.; Tarascon, J. M. Electrical energy storage for the grid: A battery of choices. *Science* **2011**, *334*, 928–935.

[2] Goodenough, J. B.; Park, K. S. The Li-ion rechargeable battery: A perspective. *J. Am. Chem. Soc.* **2013**, *135*, 1167–1176.

[3] Li, H.; Wang, Z. X.; Chen, L. Q.; Huang, X. J. Research on advanced materials for Li-ion batteries. *Adv. Mater.* **2009**, *21*, 4593–4607.

[4] Tarascon, J. M.; Armand, M. Issues and challenges facing rechargeable lithium batteries. *Nature* **2001**, *414*, 359–367.

[5] Ellis, B. L.; Makahnouk, W. R. M.; Makimura, Y.; Toghill, K.; Nazar, L. F. A multifunctional 3.5 V iron-based phosphate

cathode for rechargeable batteries. *Nat. Mater.* **2007**, *6*, 749–753.

[6] Ong, S. P.; Chevrier, V. L.; Hautier, G.; Jain, A.; Moore, C.; Kim, S.; Ma, X. H.; Ceder, G. Voltage, stability and diffusion barrier differences between sodium-ion and lithium-ion intercalation materials. *Energy Environ. Sci.* **2011**, *4*, 3680–3688.

[7] Palomares, V.; Serras, P.; Villaluenga, I.; Hueso, K. B.; Carretero-Gonzalez, J.; Rojo, T. Na-ion batteries, recent advances and present challenges to become low cost energy storage systems. *Energy Environ. Sci.* **2012**, *5*, 5884–5901.

[8] Xu, Y.; Zhou, M.; Lei, Y. Nanoarchitectured array electrodes for rechargeable lithium- and sodium-ion batteries. *Adv. Energy Mater.* **2016**, *6*, 1502514.

[9] Slater, M. D.; Kim, D.; Lee, E.; Johnson, C. S. Sodium-ion batteries. *Adv. Funct. Mater.* **2013**, *23*, 947–958.

[10] Wang, L.; Lu, Y. H.; Liu, J.; Xu, M. W.; Cheng, J. G.; Zhang, D. W.; Goodenough, J. B. A superior low-cost cathode for a Na-ion battery. *Angew. Chem., Int. Ed.* **2013**, *52*, 1964–1967.

[11] Xu, D. F.; Chen, C. J.; Xie, J.; Zhang, B.; Miao, L.; Cai, J.; Huang, Y. H.; Zhang, L. N. A hierarchical N/S-codoped carbon anode fabricated facilely from cellulose/polyaniline microspheres for high-performance sodium-ion batteries. *Adv. Energy Mater.* **2016**, *6*, 1501929.

[12] Shen, F.; Luo, W.; Dai, J. Q.; Yao, Y. G.; Zhu, M. W.; Hitz, E.; Tang, Y. F.; Chen, Y. F.; Sprenkle, V. L.; Li, X. L. et al. Ultra-thick, low-tortuosity, and mesoporous wood carbon anode for high-performance sodium-ion batteries. *Adv. Energy Mater.* **2016**, *6*, 1600377.

[13] Li, Z. F.; Ma, L.; Surta, T. W.; Bommier, C.; Jian, Z. L.; Xing, Z. Y.; Stickle, W. F.; Dolgos, M.; Amine, K.; Lu, J. et al. High capacity of hard carbon anode in Na-ion batteries unlocked by PO_x doping. *ACS Energy Lett.* **2016**, *1*, 395–401.

[14] Zhang, C.; Wang, X.; Liang, Q. F.; Liu, X. Z.; Weng, Q. H.; Liu, J. W.; Yang, Y. J.; Dai, Z. H.; Ding, K. J.; Bando, Y. et al. Amorphous phosphorus/nitrogen-doped graphene paper for ultrastable sodium-ion batteries. *Nano Lett.* **2016**, *16*, 2054–2060.

[15] Li, W. H.; Yang, Z. Z.; Li, M. S.; Jiang, Y.; Wei, X.; Zhong, X. W.; Gu, L.; Yu, Y. Amorphous red phosphorus embedded in highly ordered mesoporous carbon with superior lithium and sodium storage capacity. *Nano Lett.* **2016**, *16*, 1546–1553.

[16] Song, J. X.; Yu, Z. X.; Gordin, M. L.; Li, X. L.; Peng, H. S.; Wang, D. H. Advanced sodium ion battery anode constructed via chemical bonding between phosphorus, carbon nanotube, and cross-linked polymer binder. *ACS Nano* **2015**, *9*, 11933–11941.

[17] Li, X. F.; Dhanabalan, A.; Gu, L.; Wang, C. L. Three-dimensional porous core–shell Sn@carbon composite anodes for high-performance lithium-ion battery applications. *Adv. Energy Mater.* **2012**, *2*, 238–244.

[18] Wang, N. N.; Bai, Z. C.; Qian, Y. T.; Yang, J. Double-walled Sb@TiO_{2-x} nanotubes as a superior high-rate and ultralong-lifespan anode material for Na-ion and Li-ion batteries. *Adv. Mater.* **2016**, *28*, 4126–4133.

[19] Liang, L. Y.; Xu, Y.; Wang, C. L.; Wen, L. Y.; Fang, Y. G.; Mi, Y.; Zhou, M.; Zhao, H. P.; Lei, Y. Large-scale highly ordered Sb nanorod array anodes with high capacity and rate capability for sodium-ion batteries. *Energy Environ. Sci.* **2015**, *8*, 2954–2962.

[20] Liu, J.; Yu, L. T.; Wu, C.; Wen, Y. R.; Yin, K. B.; Chiang, F.-K.; Hu, R. Z.; Liu, J. W.; Sun, L. T.; Gu, L. et al. New nanoconfined galvanic replacement synthesis of hollow Sb@C yolk–shell spheres constituting a stable anode for high-rate Li/Na-ion batteries. *Nano Lett.* **2017**, *17*, 2034–2042.

[21] Er, D. Q.; Li, J. W.; Naguib, M.; Gogotsi, Y.; Shenoy, V. B. Ti_3C_2 MXene as a high capacity electrode material for metal (Li, Na, K, Ca) ion batteries. *ACS Appl. Mater. Interfaces* **2014**, *6*, 11173–11179.

[22] Xie, Y.; Dall'Agnese, Y.; Naguib, M.; Gogotsi, Y.; Barsoum, M. W.; Zhuang, H. L.; Kent, P. R. C. Prediction and characterization of MXene nanosheet anodes for non-lithium-ion batteries. *ACS Nano* **2014**, *8*, 9606–9615.

[23] Yu, L. T.; Liu, J.; Xu, X. J.; Zhang, L. G.; Hu, R. Z.; Liu, J. W.; Ouyang, L. Z.; Yang, L. C.; Zhu, M. Ilmenite nanotubes for high stability and high rate sodium-ion battery anodes. *ACS Nano* **2017**, *11*, 5120–5129.

[24] Xu, X. J.; Liu, J.; Liu, Z. B.; Shen, J. D.; Hu, R. Z.; Liu, J. W.; Ouyang, L. Z.; Zhang, L.; Zhu, M. Robust pitaya-structured pyrite as high energy density cathode for high-rate lithium batteries. *ACS Nano* **2017**, *11*, 9033–9040.

[25] Ye, L. N.; Wu, C. Z.; Guo, W.; Xie, Y. MoS_2 hierarchical hollow cubic cages assembled by bilayers: One-step synthesis and their electrochemical hydrogen storage properties. *Chem. Commun.* **2006**, 4738–4740.

[26] Karunadasa, H. I.; Montalvo, E.; Sun, Y.; Majda, M.; Long, J. R.; Chang, C. J. A molecular MoS_2 edge site mimic for catalytic hydrogen generation. *Science* **2012**, *335*, 698–702.

[27] Wu, W. Z.; Wang, L.; Yu, R. M.; Liu, Y. Y.; Wei, S. H.; Hone, J.; Wang, Z. L. Piezophototronic effect in single-atomic-layer MoS_2 for strain-gated flexible optoelectronics. *Adv. Mater.* **2016**, *28*, 8463–8468.

[28] Deng, Z. N.; Jiang, H.; Hu, Y. J.; Liu, Y.; Zhang, L.; Liu, H. L.; Li, C. Z. 3D ordered macroporous MoS_2@C nanostructure for flexible Li-ion batteries. *Adv. Mater.* **2017**, *29*, 1603020.

[29] Zuo, X. X.; Chang, K.; Zhao, J.; Xie, Z. Z.; Tang, H. W.; Li, B.; Chang, Z. R. Bubble-template-assisted synthesis of hollow fullerene-like MoS_2 nanocages as a lithium ion battery anode material. *J. Mater. Chem. A* **2016**, *4*, 51–58.

[30] Ding, Y.-L.; Kopold, P.; Hahn, K.; van Aken, P. A.; Maier, J.; Yu, Y. A lamellar hybrid assembled from metal disulfide nanowall arrays anchored on a carbon layer: *In situ* hybridization and improved sodium storage. *Adv. Mater.* **2016**, *28*, 7774–7782.

[31] Wang, T. Y.; Chen, S. Q.; Pang, H.; Xue, H. G.; Yu, Y. MoS_2-based nanocomposites for electrochemical energy storage. *Adv. Sci.* **2017**, *4*, 1600289.

[32] Park, J.; Kim, J.-S.; Park, J.-W.; Nam, T.-H.; Kim, K.-W.; Ahn, J.-H.; Wang, G. X.; Ahn, H.-J. Discharge mechanism of MoS_2 for sodium ion battery: Electrochemical measurements and characterization. *Electrochim. Acta* **2013**, *92*, 427–432.

[33] Xie, X. Q.; Ao, Z. M.; Su, D. W.; Zhang, J. Q.; Wang, G. X. MoS_2/graphene composite anodes with enhanced performance for sodium-ion batteries: The role of the two-dimensional heterointerface. *Adv. Funct. Mater.* **2015**, *25*, 1393–1403.

[34] Ren, W. N.; Zhang, H. F.; Guan, C.; Cheng, C. W. Ultrathin MoS_2 nanosheets@metal organic framework-derived N-doped carbon nanowall arrays as sodium ion battery anode with superior cycling life and rate capability. *Adv. Funct. Mater.* **2017**, *27*, 1702116.

[35] Zhang, X. Q.; Li, X. N.; Liang, J. W.; Zhu, Y. C.; Qian, Y. T. Synthesis of MoS_2@C nanotubes via the kirkendall effect with enhanced electrochemical performance for lithium ion and sodium ion batteries. *Small* **2016**, *12*, 2484–2491.

[36] Chang, K.; Chen, W. X. L-cysteine-assisted synthesis of layered MoS_2/graphene composites with excellent electrochemical performances for lithium ion batteries. *ACS Nano* **2011**, *5*, 4720–4728.

[37] Yu, X. Y.; Hu, H.; Wang, Y. W.; Chen, H. Y.; Lou, X. W. D. Ultrathin MoS_2 nanosheets supported on N-doped carbon nanoboxes with enhanced lithium storage and electrocatalytic properties. *Angew. Chem., Int. Ed.* **2015**, *54*, 7395–7398.

[38] Xu, X.; Fan, Z. Y.; Ding, S. J.; Yu, D. M.; Du, Y. P. Fabrication of MoS_2 nanosheet@TiO_2 nanotube hybrid nanostructures for lithium storage. *Nanoscale* **2014**, *6*, 5245–5250.

[39] Liu, H.; Su, D. W.; Zhou, R. F.; Sun, B.; Wang, G. X.; Qiao, S. Z. Highly ordered mesoporous MoS_2 with expanded spacing of the (002) crystal plane for ultrafast lithium ion storage. *Adv. Energy Mater.* **2012**, *2*, 970–975.

[40] Wang, Y.; Qu, Q. T.; Li, G. C.; Gao, T.; Qian, F.; Shao, J.; Liu, W. J.; Shi, Q.; Zheng, H. H. 3D interconnected and multiwalled carbon@MoS_2@carbon hollow nanocables as outstanding anodes for Na-ion batteries. *Small* **2016**, *12*, 6033–6041.

[41] Shi, Z.-T.; Kang, W. P.; Xu, J.; Sun, Y.-W.; Jiang, M.; Ng, T.-W.; Xue, H.-T.; Yu, D. Y. W.; Zhang, W. J.; Lee, C.-S. Hierarchical nanotubes assembled from MoS_2-carbon monolayer sandwiched superstructure nanosheets for high-performance sodium ion batteries. *Nano Energy* **2016**, *22*, 27–37.

[42] Park, S.-K.; Lee, J.; Bong, S.; Jang, B.; Seong, K.-D.; Piao, Y. Z. Scalable synthesis of few-layer MoS_2 incorporated into hierarchical porous carbon nanosheets for high-performance Li- and Na-ion battery anodes. *ACS Appl. Mater. Interfaces* **2016**, *8*, 19456–19465.

[43] Wang, M.; Yang, Z. Z.; Li, W. H.; Gu, L.; Yu, Y. Superior sodium storage in 3D interconnected nitrogen and oxygen dual-doped carbon network. *Small* **2016**, *12*, 2559–2566.

[44] Huang, Y.; Lin, Z. X.; Zheng, M. B.; Wang, T. H.; Yang, J. Z.; Yuan, F. S.; Lu, X. Y.; Liu, L.; Sun, D. P. Amorphous Fe_2O_3 nanoshells coated on carbonized bacterial cellulose nanofibers as a flexible anode for high-performance lithium ion batteries. *J. Power Sources* **2016**, *307*, 649–656.

[45] Wang, M.; Yang, Y.; Yang, Z. Z.; Gu, L.; Chen, Q. W.; Yu, Y. Sodium-ion batteries: Improving the rate capability of 3D interconnected carbon nanofibers thin film by boron, nitrogen dual-doping. *Adv. Sci.* **2017**, *4*, 1600468.

[46] Hu, Z.; Wang, L. X.; Zhang, K.; Wang, J. B.; Cheng, F. Y.; Tao, Z. L.; Chen, J. MoS_2 nanoflowers with expanded interlayers as high-performance anodes for sodium-ion batteries. *Angew. Chem., Int. Ed.* **2014**, *126*, 13008–13012.

[47] Xie, X. Q.; Makaryan, T.; Zhao, M. Q.; Van Aken, K. L.; Gogotsi, Y.; Wang, G. X. MoS_2 nanosheets vertically aligned on carbon paper: A freestanding electrode for highly reversible sodium-ion batteries. *Adv. Energy Mater.* **2016**, *6*, 1502161.

[48] Liu, Y. P.; He, X. Y.; Hanlon, D.; Harvey, A.; Coleman, J. N.; Li, Y. G. Liquid phase exfoliated MoS_2 nanosheets percolated with carbon nanotubes for high volumetric/areal capacity sodium-ion batteries. *ACS Nano* **2016**, *10*, 8821–8828.

[49] Wang, R. H.; Xu, C. H.; Sun, J.; Liu, Y. Q.; Gao, L.; Yao, H. L.; Lin, C. C. Heat-induced formation of porous and free-standing MoS_2/GS hybrid electrodes for binder-free and ultralong-life lithium ion batteries. *Nano Energy* **2014**, *8*, 183–195.

[50] Yu, Z. L.; Xin, S.; You, Y.; Yu, L.; Lin, Y.; Xu, D. W.; Qiao, C.; Huang, Z. H.; Yang, N.; Yu, S. H. et al. Ion-catalyzed synthesis of microporous hard carbon embedded with expanded nanographite for enhanced lithium/sodium storage. *J. Am. Chem. Soc.* **2016**, *138*, 14915–14922.

[51] Wang, Y.; Wang, C. Y.; Wang, Y. J.; Liu, H. K.; Huang, Z.

G. Boric acid assisted reduction of graphene oxide: A promising material for sodium-ion batteries. *ACS Appl. Mater. Interfaces* **2016**, *8*, 18860–18866.

[52] Wang, Y. S.; Ma, Z. M.; Chen, Y. J.; Zou, M. C.; Yousaf, M.; Yang, Y. B.; Yang, L. S.; Cao, A. Y.; Han, R. P. S. Controlled synthesis of core–shell carbon@MoS_2 nanotube sponges as high-performance battery electrodes. *Adv. Mater.* **2016**, *28*, 10175–10181.

[53] Wang, J.; Liu, J. L.; Yang, H.; Chao, D. L.; Yan, J. X.; Savilov, S. V.; Lin, J. Y.; Shen, Z. X. MoS_2 nanosheets decorated Ni_3S_2@MoS_2 coaxial nanofibers: Constructing an ideal heterostructure for enhanced Na-ion storage. *Nano Energy* **2016**, *20*, 1–10.

[54] Mahmood, Q.; Park, S. K.; Kwon, K. D.; Chang, S. J.; Hong, J. Y.; Shen, G. Z.; Jung, Y. M.; Park, T. J.; Khang, S. W.; Kim, W. S. et al. Transition from diffusion-controlled intercalation into extrinsically pseudocapacitive charge storage of MoS_2 by nanoscale heterostructuring. *Adv. Energy Mater.* **2016**, *6*, 1501115.

[55] Wang, J. J.; Luo, C.; Gao, T.; Langrock, A.; Mignerey, A. C.; Wang, C. S. An advanced MoS_2/carbon anode for high-performance sodium-ion batteries. *Small* **2015**, *11*, 473–481.

[56] Choi, S. H.; Ko, Y. N.; Lee, J.-K.; Kang, Y. C. 3D MoS_2-graphene microspheres consisting of multiple nanospheres with superior sodium ion storage properties. *Adv. Funct. Mater.* **2015**, *25*, 1780–1788.